Ultrasonics Sonochemistry 78 (2021) 105750

Contents lists available at ScienceDirect

Ultrasonics Sonochemistry

journal homepage: www.elsevier.com/locate/ultson

Ultrasonic role to activate persulfate/chlorite with foamed zero-valent-iron: Sonochemical applications and induced mechanisms

Qihui Xu [a], Hong Zhang [b], Haoran Leng [a], Hong You [a,b,*], Yuhong Jia [b], Shutao Wang [a]

[a] State Key Laboratory of Urban Water Resources and Environment, Harbin Institute of Technology, Harbin 150090, China
[b] School of Marine Science and Technology, Harbin Institute of Technology at Weihai, Weihai 264209, China

ARTICLE INFO

Keywords:
Persulfate/chlorite composite oxidants
Ultrasonic role
Polishing zero-valent iron foam
Determining active species

ABSTRACT

The novel system, consisting of composite oxidants (persulfate/chlorite, $S_2O_8^{2-}$/ClO_2^-) and stationary phase activator (zero-valent-iron foam, Fe^0_f) driven by ultrasonic (US) field, was applied to treat the triphenylmethane derivative effectively even at low temperature (≈ 289 K). By comparisons of sub-systems, the US roles to $S_2O_8^{2-}$, ClO_2^-, and Fe^0_f were seriatim analyzed. US made the reaction order of multi-component system tend to within 1 (leading to de-order reaction), and widened pH activating range of the Fe^0_f by sonicate-polishing during the process of ClO_2^- co-activating $S_2O_8^{2-}$. US and Fe^0_f were affected by fluid eddy on activating $S_2O_8^{2-}$/ClO_2^-. The Fe^0_f had slight effect on the temperature of US bubble-water interface but the addition of ClO_2^- lowered it. The partitioning capacity of the above US reactive zone increased during the reaction. US and ClO_2^- could enrich the kinds of degradation intermediates. The contributions of free radicals (ClO_x-based radicals, sulfate radicals ($SO_4^{\bullet-}$), and hydroxyl radicals (•OH)) and non-free radicals (ClO_2, and $O=Fe^{IV/V}$ from ionic Fe under "-O-O-" of $S_2O_8^{2-}$ and cyclic adjustment reaction of ClO_2^-) processes by sonochemical induction were equally important by corresponding detection means. Especially, real-time and online high-resolution mass spectrum by self-developing further confirmed the chain transfers of different free radicals due to US role. The findings expanded the application of sono-persulfate-based systems and improved understanding on activation mechanism.

1. Introduction

A series of trace triphenylmethane derivatives detected in aquatic environment with low concentration (<μM level) as emerging contaminants have drawn the attention [1], therein no lack of triphenylmethane crystal-violet (tpm_{CV}). Besides as the dye, the tpm_{CV} (Fig. S1a), could be used not only in clinical treatment, but also as antimicrobial and antiparasitic agents in aquaculture to treat and prevent fungal and protozoal infections [2]. However, the United States, the European Union, China, and others have not approved the use of tpm_{CV} in aquaculture due to it with the possible carcinogen, mutagen and teratogen effects [1–3]. Even so, the use of the prohibited and persistent tpm_{CV} would be common occurance, leading to its frequent detection in aquatic environment. Specially, the bio-concentration of organisms made tpm_{CV} convert into leuco crystal-violet ($_Ltpm_{CV}$, Fig. S1b) (more toxic and more difficult to be metabolized) [1,3], which might be seen as the persistent pollutants.

$$H_2O \overset{))))}{\rightarrow} \bullet OH + \bullet H \quad (1)$$

The alternative US-based advanced oxidation processes (AOPs), as the promising and friendly treatment technologies with physicochemical processes of cavitation (gas-phase reaction zone effective temperature, ≈ 5200 K, and high pressure, in the range of hundreds of bars), pyrolysis (breaking chemical bonds, and yielding hydroxyl radicals (Eq. (1)) [4]), supercritical water oxidation (depth and temperature of the liquid-phase reaction zone, ≈ 0.2 μm and ≈ 1900 K, respectively), and violent turbulence [5,6]; meanwhile, especially as the sono-catalysis technologies to activate oxidizing agents to produce active species to form combined system [5–7], have attracted particular concern for environmental remediation. Herein, as a kind of oxidizing agent, persulfate (involving peroxymonosulfate (HSO_5^-, PMS) or peroxydisulfate ($S_2O_8^{2-}$, PDS)) with direct oxidizing or producing $SO_4^{\bullet-}$ (E^0 ($SO_4^{\bullet-}$/SO_4^{2-}) = 2.60 – 3.10 V_{NHE}) by activation to improve the oxidizing capacity [8] via physicochemical means (e.g. alkali, Eq. (2); heat, Eq. (3) [9]; photo-; electro-; microwave; and US, Eq. (4)), metal-free catalysis

* Corresponding author at: State Key Laboratory of Urban Water Resources and Environment, Harbin Institute of Technology, Harbin 150090, China.
E-mail address: youhong@hit.edu.cn (H. You).

https://doi.org/10.1016/j.ultsonch.2021.105750
Received 22 June 2021; Received in revised form 31 August 2021; Accepted 4 September 2021
Available online 10 September 2021

[10], metal-based materials (e.g. zero-valence metal, Eq. (5)) [11], and other methods (e.g. ozone, superoxide, and plasma), could be used to treat environmental contaminants as well.

$$2S_2O_8^{2-} + 2H_2O \xrightarrow{OH^-} SO_4^{\bullet -} + O_2^{\bullet -} + 3SO_4^{2-} + 4H^+ \quad (2)$$

$$S_2O_8^{2-} \xrightarrow{\text{heat}} 2SO_4^{\bullet -} \quad k = 1.0 \times 10^{-7} s^{-1} \ (298\ K) \text{ or } 5.7 \times 10^{-5} s^{-1} \ (343\ K) \quad (3)$$

$$S_2O_8^{2-} \xrightarrow{h\nu/))))} 2SO_4^{\bullet -} \quad (4)$$

$$\equiv M^{n+} + S_2O_8^{2-} \rightarrow \equiv M^{(n+1)+} + SO_4^{2-} + SO_4^{\bullet -} \quad (5)$$

Therefore, further works for sono-persulfate based AOPs were worth exploring to extend acoustic catalysis and persulfate activation bilaterally, seeming to become prospective treatment methods for the elimination of refractory organic contaminants above.

At present, the zero-valent-iron (ZVI, Fe^0)-based materials in disperse mediums by modified techniques (pre-magnetized [12], sulfidated [13], loaded/embedded [14], micro/nano [15]) or in stationary phase ZVI (e.g. foamed-ZVI (Fe^0_f) consisting of three-dimensional porous form (Fig. S1c) with properties [16,17] of permeability, controlled pore size, foveolate structure, shape stability, and machinability) as the activated intermediary to connect the US and persulfate, have obtained great attention. Herein, the Fe^0_f for oxidant activation was rarely reported, however, functional materials based on Fe^0_f have drawn important attention, such as, electrode materials for hydrogen evolution reaction or oxygen evolution reaction (electrocatalytic water splitting) [17], which also had greater potential for environmental remediation. However, the surface passivation of ZVI has been a fatal problem affecting its activation to persulfate. Nevertheless, it's just that introducing US could polish the above ZVI in activation process, and ease the burden of passivation to provide the fresh ZVI.

In addition, in order to promote corrosion of ZVI and regulate the activation cycle (e.g. ionic Fe cycle) under the action of US, the chlorite (ClO_2^-, Cl(III)) could be introduced into the aforementioned process and combined with persulfate to form composite oxidants. Commonly, ClO_2^- with a higher quantum yield at 254 nm, 1.0–1.53 mol·Einstein^{-1} [18,19], comparing with H_2O_2 (0.5 mol·Einstein^{-1}) and persulfate (0.7 mol·Einstein^{-1}) [20], could be activated by physical fields including UV-light stimuli ([18], Eq. (6)), heat [21], and US, or chemical agents including acid (Eq. (7)) and PDS [22] to produce chlorine dioxide (ClO_2).

$$3ClO_2^- + H_2O \xrightarrow{h\nu} 2ClO_2 + Cl^- + 2OH^- + 0.5O_2 \quad (6)$$

$$5ClO_2^- + 4H^+ \rightarrow Cl^- + 4ClO_2 + 2H_2O \quad (7)$$

The ensuing surface passivation of ZVI (Cl role) may impede its further activation, however, introducing US, as a "bridge", could not only activate composite oxidants, persulfate/chlorite (O_{SC}), to generate $SO_4^{\bullet -}$ and ClO_2 by co-catalysis (Eq. (8)) [23], but also polish the Fe^0_f to avoid aforementioned Fe^0_f passivation and to activate O_{SC} deeply (Eqs. (9)-(13)).

$$S_2O_8^{2-} + ClO_2^- \xrightarrow{))))} SO_4^{\bullet -} + SO_4^{2-} + ClO_2 \quad (8)$$

$$Fe^0_f + S_2O_8^{2-} \rightarrow Fe^{II} + 2SO_4^{2-} \quad (9)$$

$$Fe^{II} + S_2O_8^{2-} \rightarrow Fe^{III}_{(aq\&s)} + SO_4^{\bullet -} + SO_4^{2-} \quad (10)$$

$$Fe^{II} + ClO_2 \rightarrow Fe^{III}_{(aq\&s)} + ClO_2^- \quad (11)$$

$$4Fe^{II} + ClO_2^- + 2H_2O \rightarrow 4Fe^{III}_{(aq\&s)} + Cl^- + 4OH^- \quad (12)$$

$$2Fe^{III}_{(aq)} + polished Fe^0_f \rightarrow 3Fe^{II} \quad (13)$$

In this study, the novel treatment systems, namely, the combined system (US/Fe^0_f-O_{SC}) based on co-catalysis involving acoustic catalysis and multiple activation of composite oxidants, and sub-systems, were established. The commonly apparent effects of US may have been mentioned, however, because of that US has always been seemed as just an assistant method in environmental remediation, the researches on its applied potential (e.g. couple function as a "bridge" of systems above by series connection) and feasible mechanism of US role (e.g. US role to transformations of generated active species) may be neglected.

This study was therefore designed to (1) evaluate applications of the combined- and sub- systems based on US from comparisons of performances, affecting parameters, and pollutant degradation paths; (2) reveal the detailed sonochemical roles in apparent remediation by comparisons of coupling systems; and (3) explore the roles of US-induction in remediation mechanism by comparisons of free radicals and non-free radicals processes.

2. Experiment

2.1. Operating

The operating processes including chemicals, self-developed US/catalytic/activated reactors (UCARs), etc. were presented in Section **S1**.

2.2. Analytical methods

The intermediates of tpm_{CV} and methyl phenyl sulfoxide (PMSO) were detected by gas chromatograph-mass spectrometer (GC/MS, Trace 1300 ISQ-QD, Thermo Fisher). The temperature programming (GC/MS) was: column temperature 323 K, hold time 3 min; 10 K·min^{-1} up to 573 K, hold time 10 min. Before the above analysis, 50 mL subsample at a certain treating time (5, 15, 25, 35, and 45 min) was extracted with 15 mL dichloromethane, respectively. Afterward, the extracted solution by mixing was dehydrated by anhydrous sodium sulfate and concentrated to 2 mL. The ClO_2 and tpm_{CV} concentration were detected by UV–vis spectrum (TU-1810S, PGENERAL, China) at 360 nm [19] and 584 nm, respectively. The concentrations of "Fe" were determined by phenanthroline spectrophotometry at 510 nm (HJ/T 345–2007). The accurate acoustic-intensity entering the system was measured by the calorimetry method [24], presenting in Section **S2** (Eq. S1). The compositions and micrographs of the Fe^0_f, before and after treatment, were detected and examined by X-ray diffraction (XRD, HAOYUAN Instrument, DX-2700) and scanning electron microscopy (SEM, Zeiss, Germany), respectively. Before XRD and SEM, the Fe^0_f samples taken out from reaction solution needed dehydration immediately by adding into absolute ethyl alcohol, then drying out with filter papers, finally vacuum drying. The anions of $S_2O_8^{2-}$/ClO_2^- were detected by ion chromatography (IC, ThermoScientific, Aquion).

2.3. Spin trapping and EPR measurements

The US filed was applied in solution consisting of $NaClO_2$ (1–20 mM) and $K_2S_2O_8$ (ClO_2^-: $S_2O_8^{2-}$ = 1:5 in molar ratio) to conduct sonochemical experiments, then Fe^0_f was added as needed. DMPO with equal proportion of O_{SC} was utilized to trap the generated active species above. In addition, dimethyl sulfoxide (DMSO, as needed) was added into water to form mixture for comparison.

The electron paramagnetic resonance (EPR) spectra were obtained by a Bruker A200 spectrometer. General instrument settings were as follows unless otherwise noted: center field 3490 G, modulation frequency 100 kHz, modulation amplitude 1 G, receiver gain 1.42 × 10^4, time constant 20.5 ms, conversion time 40 ms, sweep time 41 s, frequency 9.82 GHz, and power 19.47 mW. The hyperfine splitting constants were measured by using Bruker Win-EPR SimFonia (Version 1.2).

2.4. Real-time and online continuous detection

In Scheme 1, the real-time and online continuous (ROC) detections of reaction mixtures were realized with a self-developed pneumatic nebulization (PN)-droplet spray ionization (DSI) (electrospray ionization (ESI) with CH_3OH as an assist as required) coupled to LTQ and LTQ-Orbitrap high resolution mass spectrum (HRMS) (Thermo Scientific) in positive or negative mode with a resolution of 60 000. Online MS/MS analysis of the captured intermediates could be performed during the reaction process. Data were acquired in full scan in the *m/z* range 50–300 and in MS/MS with a collision-induced dissociation energy of 25. The instrument was calibrated routinely with the provided calibration solution by Thermo Scientific to ensure mass accuracy within ± 3 ppm.

The self-developed PN-DSI as Scheme 1① shown: the sealed glass device (7 mL) was equipped with mixture (5 mL) of $S_2O_8^{2-}$ at 5×10^{-6} M, ClO_2^- at 1×10^{-6} M, and DMPO at 1×10^{-4} M under US generator; then the liquid along the capillary tube entered into the site of triple valve by N_2 inflating; and the charged samples from the above liquid, suffering the action of PN (its description in Section **S3**) by another N_2 flow, were transmitted into HRMS.

2.5. Simulation on US reactor

The Acoustic-Piezoelectric Interaction of COMSOL Multiphysics, including pressure acoustics Eq. (14), was applied to simulate heterogeneous reaction process and visualize the action of US-field in the solution. The detailed simulation process were described in Section **S4** (Eqs. S2-S25). The UCAR2 was simulated as shown in Fig. 1a-c and Fig. S2a-g.

$$\nabla \cdot \left(-\frac{1}{\rho_c}(\nabla p_t - \boldsymbol{q}_d) \right) - \frac{k_{eq}^2 p_t}{\rho_c} = Q_m \tag{14}$$

3. Results and discussion

3.1. Comparisons of US-based systems

At low temperature (≈ initial 289 K), low pollutant concentration (10^{-6} M, μM level), and near-neutral pH (without adjustment), the novel US/Fe^0_f-O_{SC} presented good performance on removing tpm_{CV}. O_{SC}, consisting of $S_2O_8^{2-}$ and ClO_2^- with molar ratio 5:1, was sourced from our previous study. From Fig. 1d, the treating efficiencies of tpm_{CV} by US/O_{SC} (6 mM)-based systems were greater than those by US/PDS (6 mM)-based systems, due to the degradation of tpm_{CV} in US/PDS-based systems presenting weak implementation on activation in later stage (e.g. after 15 min).

The exponential analysis of apparent dynamics could be utilized to further understand the removal process of tpm_{CV} (details in Section **S5**, Eqs. S26-S28). By fitting concentration functions of the systems mentioned above, the optimal fitting orders (non-integer, $R^2_{Adj} > 0.999$, Fig. 1e) of O_{SC}, Fe^0_f-O_{SC}, US-O_{SC}, and US/Fe^0_f-O_{SC} systems were 1.35, 1.10, 0.90, and 0.75, respectively.

In order to further measure the synergistic effect among the above-mentioned systems (Fig. 1e) conveniently, the S and f_i (details in Section **S6**, Eqs. S29-S33) were calculated to evaluate interactions of each O_{SC}-based system with pseudo-first-order kinetics ($R^2_{Adj} > 0.990$) as below (k_{obs} values (10^{-3}, min^{-1}) of O_{SC}, Fe^0_f-O_{SC}, US-O_{SC}, and US/Fe^0_f-O_{SC} systems: 46.82, 51.56, 57.22, and 85.64, respectively).

$$S = \frac{k_{obsn}}{\sum k_{obsi}} \tag{15}$$

$$f_i = \frac{k_{obsn}}{k_{obsn-1}} \tag{16}$$

where S is the synergistic effect of the multicomponent system, f_i is the action of single i system, and k_{obs} represents pseudo-first-order kinetic constant unless otherwise indicated.

The S was 1.83 (>1), and the f_{US} and f_{Fe0f} in US/Fe^0_f-O_{SC} (1.66, 1.50) > those in US-O_{SC} (1.22, 1.10), which indicated that: i) US/Fe^0_f-O_{SC} had well synergistic effect; ii) The action of US was slightly better than that of Fe^0_f; iii) Compared with dual systems, both action of US and Fe^0_f enlarged in ternary systems (further confirming their synergistic effect).

In addition, the adding of US (or ClO_2^-) may enrich the varieties and amounts of active substances in the reaction system, which greatly weakened the influence of pollutant concentration, leading to de-order reaction, but Fe^0_f alone seemed to play not obvious role on the above.

3.2. Effects of factors

3.2.1. Effect of pH with/without US

The pH values greatly affected the systems of Fe^0_f-O_{SC} and US/Fe^0_f-O_{SC} on removing tpm_{CV} (Fig. 2a). Generally, the acidic condition was beneficial for degradation. After introducing US, organic pollutants could evaporate into the cavitation bubbles easily, and then be pyrolyzed directly in them under acid condition. Since pH decreased from 11 to 2, the k_{obs} (10^{-3}, min^{-1}) increased from 41.37 to 345.80 (from 38.54 to 132.73) of US/Fe^0_f-O_{SC} (Fe^0_f-O_{SC}). However, due to US role, the pH application rage of system widened (specifically, the k_{obs} of Fe^0_f-O_{SC} at pH 2 ≈ that of US/Fe^0_f-O_{SC} at pH 4; the k_{obs} of Fe^0_f-O_{SC} at pH 6.8 ≈ that of US/Fe^0_f-O_{SC} at pH 10.1) as shown in embedded Fig. 2a. Meanwhile, when pH presented alkaline, the reaction rate both in Fe^0_f-O_{SC} and US/

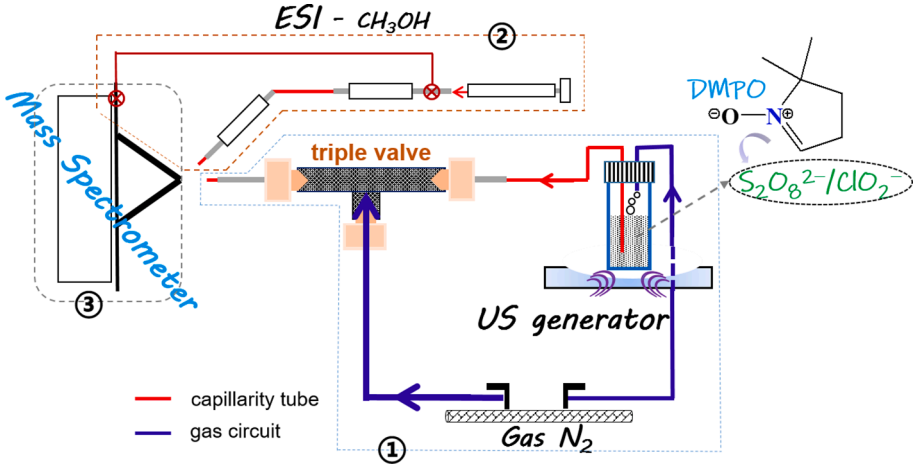

Scheme 1. Schematic diagram of ROC detection device.

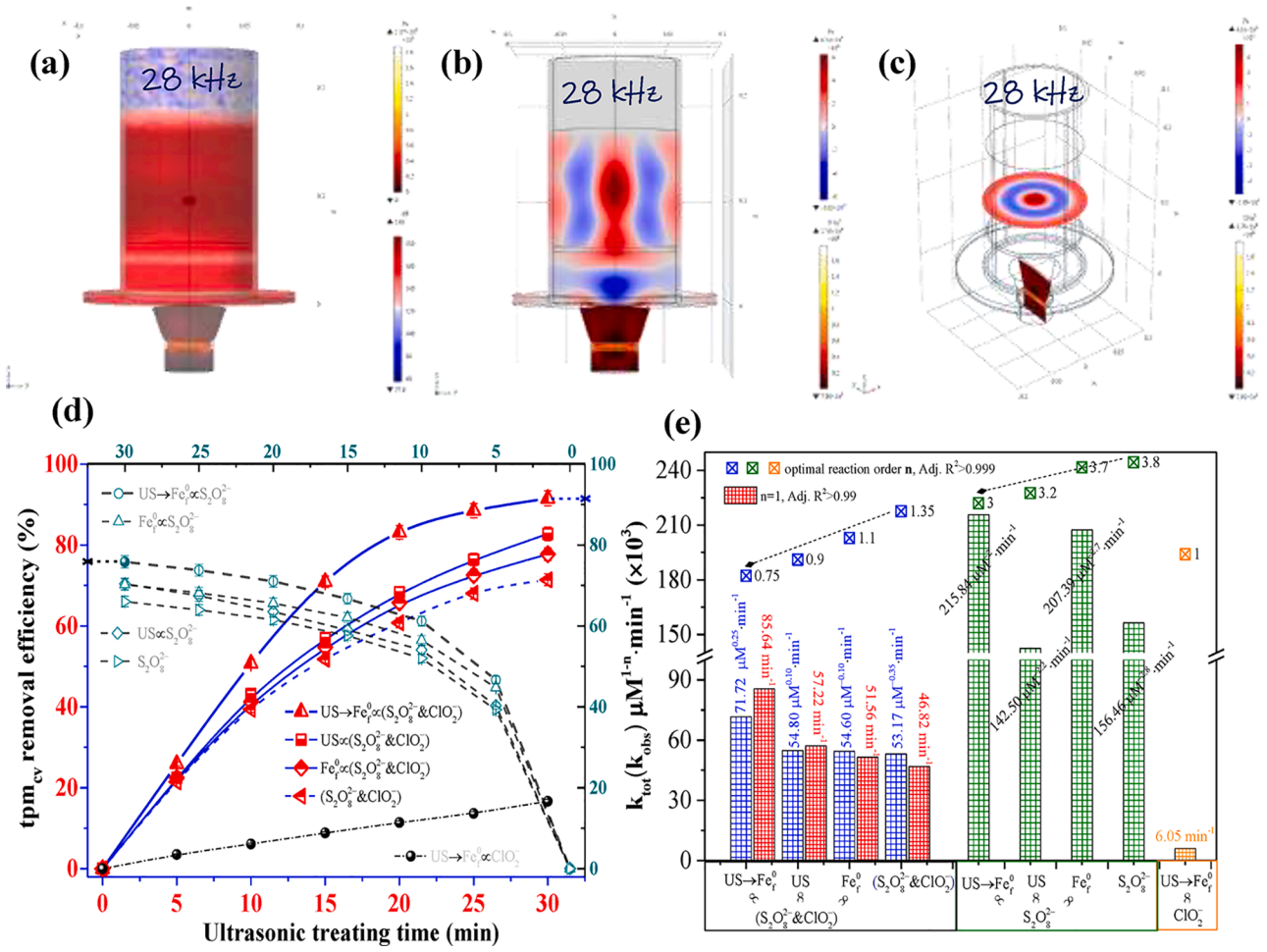

Fig. 1. Simulation of acoustic pressure distribution and piezoelectric mechanics deformation at 28 kHz with Fe^0_f: (a) sound pressure level, (b) vertical slice, (c) horizontal slice; and comparisons of O_{SC} (6 mM)-based systems and PDS (6 mM)-based systems: (d) removal efficiencies, (e) fitting kinetics ($_{molar\ ratio}S_2O_8^{2-}/ClO_2^-$ 5:1, f 28 kHz, I 30 W·L^{-1}, pH without adjustment (initial pH 6.5, near-neutral), Fe^0_f 0.358 mM, tpm_{CV} 26.47 μM, 0 r·min^{-1}, and initial T 289 K).

Fe^0_f-O_{SC} seemed to be accelerated, but it would decelerate. The greater the alkaline, the more obvious the above-mentioned phenomenon, which could be ascribed to ClO_2^- (alkali activation to form ClO• being different from acidic reaction to generate ClO_2) [20,22]. The $S_2O_8^{2-}$ was dominant, thus the alkali role to ClO_2^- could not sustain over the whole reaction process. Due to US polishing (comparing the Fig. 3) and ClO_2^- co-catalysis, the systems actually kept certain ability of treatment, and the passivation of Fe^0_f obtained remission.

3.2.2. Effect of fluid eddy with/without US

The fluid eddy was realized by mechanical mixing. The liquid height [4] was determined based on the wavelength (λ) of the applied frequency (f), namely, $\lambda = c_s/f$ where c_s was obtained as 1469.60 m·s^{-1} with the modified temperature equation (Eq. S34). The site of mechanical mixing was placed at 1/2λ (distance from bottom) [5]. In order to describe the inherent attribute of fluid by the action of mechanical mixing, herein, the angular momentum (L), moment of inertia (I_v), and rotational kinetic energy (E_{rot}) were introduced to describe the role of fluid eddy with following Eqs. S35-S37 (Section **S7**).

By comparison of Fe^0_f-O_{SC} and US/Fe^0_f-O_{SC} systems in Fig. 2b, the fluid eddy both affected the removal of tpm_{CV} varying in three stages (increased → decreased → restrained), which was partly consistent with the study of [5]. The difference was that the introduction of O_{SC} (especially, ClO_2^-) and Fe^0_f led to the appearance of restrained stage. Enlarging the fluid eddy made $S_2O_8^{2-}$ and ClO_2^- react preferentially to consume themselves by Eq. (17) (sonic catalysis weakening) and accelerate Fe^0_f surface oxidation (O_{SC} and O_2) and even passivation.

$$S_2O_8^{2-} + 2ClO_2^- \rightarrow 2SO_4^{2-} + 2ClO_2 \quad (17)$$

Due to the action of US, the peak-shift (a right-ward shift) occurred in terms of variation of k_{obs}. The enhancement in the sonochemical oxidation was attributed mainly to the direct disturbance of the ultrasound transmission and the resulting change in the cavitation-active zone.

3.2.3. Effect of initial temperature with US

The temperature affected the performance of US/Fe^0_f-O_{SC} on removing tpm_{CV} (k_{obs}, (10^{-3}, min^{-1}) increasing from 85.64 to 309.47 when T increasing from 289 K to 318 K in Fig. 2c). The reaction thermodynamics of tpm_{CV} removal was described by Eyring equation (Eqs. (18) and (19)) and Arrhenius equation (Eq. (20)) to obtain the experimentally derived free energy of activation ($\Delta G^{\neq}$), fitted enthalpy ($\Delta H^{\neq}$), entropy ($\Delta S^{\neq}$) of activation, and activation energy (E_a), respectively.

$$k_{obs} = \frac{k_b T}{h} e^{-(\Delta G^{\neq}/RT)} \quad (18)$$

$$\Delta G^{\neq} = \Delta H^{\neq} - T \times \Delta S^{\neq} \quad (19)$$

$$k_{obs} = A e^{-(E_a/RT)} \quad (20)$$

where R is the gas constant (8.314 J·mol^{-1}·K^{-1}); k_b is the Boltzmann constant (1.38×10^{-23} J·K^{-1}); h is the Planck's constant (6.626×10^{-34}

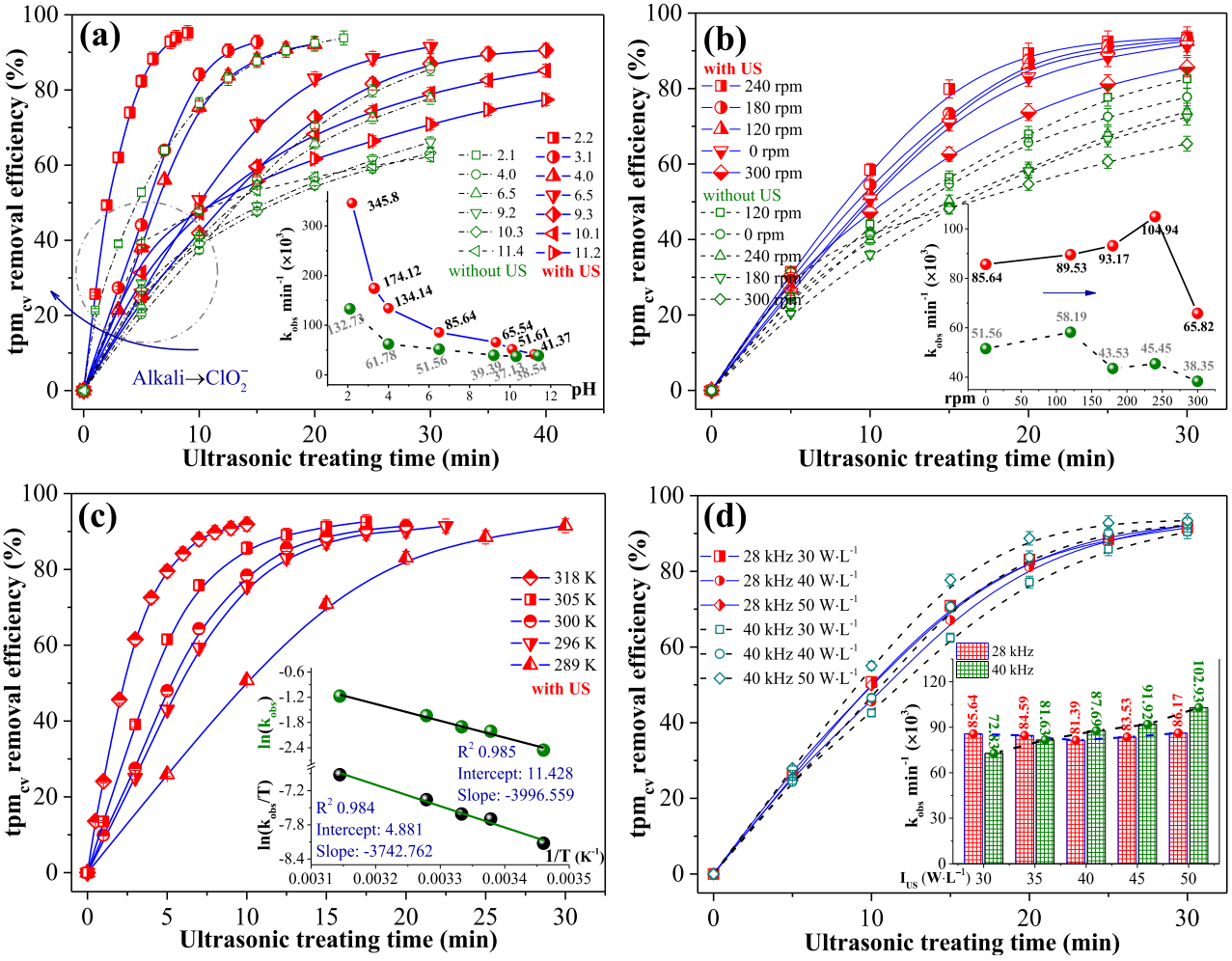

Fig. 2. Effects of (a) acid-base (comparisons of US/Fe^0_f-O_{SC} and Fe^0_f-O_{SC}), (b) fluid eddy (ibid. (a)), (c) temperature, and (d) ultrasonic intensity & frequency (basic conditions referring to Fig. 1).

J·s); and the above equations were extended in Section **S8** (Eqs. S38 and S39).

As shown in Fig. 2c, the liner relation in $\ln(k_{obs}/T)$ vs. 1/T (R^2_{Adj} = 0.984) and $\ln(k_{obs})$ vs. 1/T (R^2_{Adj} = 0.985). Therefore, the $\Delta H^{\neq}$, $\Delta S^{\neq}$, E_a, and A were calculated as 31.117 kJ·mol^{-1}, −156.956 J·mol^{-1}·K^{-1}, 33.227 kJ·mol^{-1}, and 91.858 × 10^3, respectively. Therefore, for US/Fe^0_f-O_{SC} system, the relationships ($\Delta G^{\neq}$ vs. T and k_{obs} vs. T) were expressed as $\Delta G^{\neq}$= 31.117 + 0.157 T (kJ·mol^{-1}) and k_{obs} = 9.186 × 10^{4}exp(–33.227 × 10^3/RT) (min^{-1}).

3.2.4. *Effect of US intensity and frequency*

The effects of ultrasonic intensity and frequency (Fig. 2d) were discussed in Section **S9**.

3.3. *Comparative analysis of degradation intermediates with/without US*

In terms of US/Fe^0_f-O_{SC}, mono-(S1-S13), di-(D1-D9), and tri-(T1-T4) phenylic compounds (Table S1) were detected. Comparing with double-systems Fe^0_f-O_{SC} and US-O_{SC}, the US/Fe^0_f-O_{SC} seemed to make the intermediates more diversified (Fig. S3) [25], especially, to produce more Cl-adducts (because of ClO_2^-) [22] and mono-benzene compounds (Fig. 4a) [26]. The detailed analysis was shown in Section **S10**.

3.4. *Assessing US bubble/water interface*

The k_{obs} could be measured at the macro-level based on the total UCAR solution. However, in order to obtain concrete rate constants for catalyactivation according to effectively reactive volume (k_{int} at bubble–liquid interface zone of cavitation nucleus where the reaction sites for catalysis and activation of US (or Fe^0_f) to O_{SC} (or PDS) mainly located), the mass balance expression, as Wei et al. [27] mentioned, could be used to make a conversion from k_{obs} to k_{int}:

$$k_{int} = \frac{V_{total}}{V_{int}} k_{obs} \quad (21)$$

where k_{int} was the rate constant at the phase interface, V_{total} was the volume of wastewater in treatment, and V_{int} was the volume of interfacial shell surrounding cavitation bubbles. Here, assuming the interface thickness was 10% of the radius of the cavitating bubble: an empirical value of V_{total}/V_{int} was obtained from the calculation of [27].

The effective mean temperature of the interfacial region was estimated by k_{int} and Arrhenius equation. The Arrhenius parameters (lnA = 36.6 and E_a = 134 kJ·mol^{-1}) were referred to the study of thermal dissociation of PS [27,28]. Therefore, at optimal degradation order, the corresponding temperatures of US/Fe^0_f-O_{SC}, US-O_{SC}, US/Fe^0_f-PDS, and US-PDS were calculated to be 531 K, 535 K, 737 K, and 744 K, respectively, which illustrated that i) Fe^0_f had slight effect on the interface temperature; ii) ClO_2^- lowered the interface temperature. Although the interfacial zone would have a steep temperature gradient between the hot cavitation bubble and the ambient temperature of the bulk solution [27], the calculated temperatures above could be considered as the mean effective temperatures of the interfacial region for O_{SC} (or PDS)

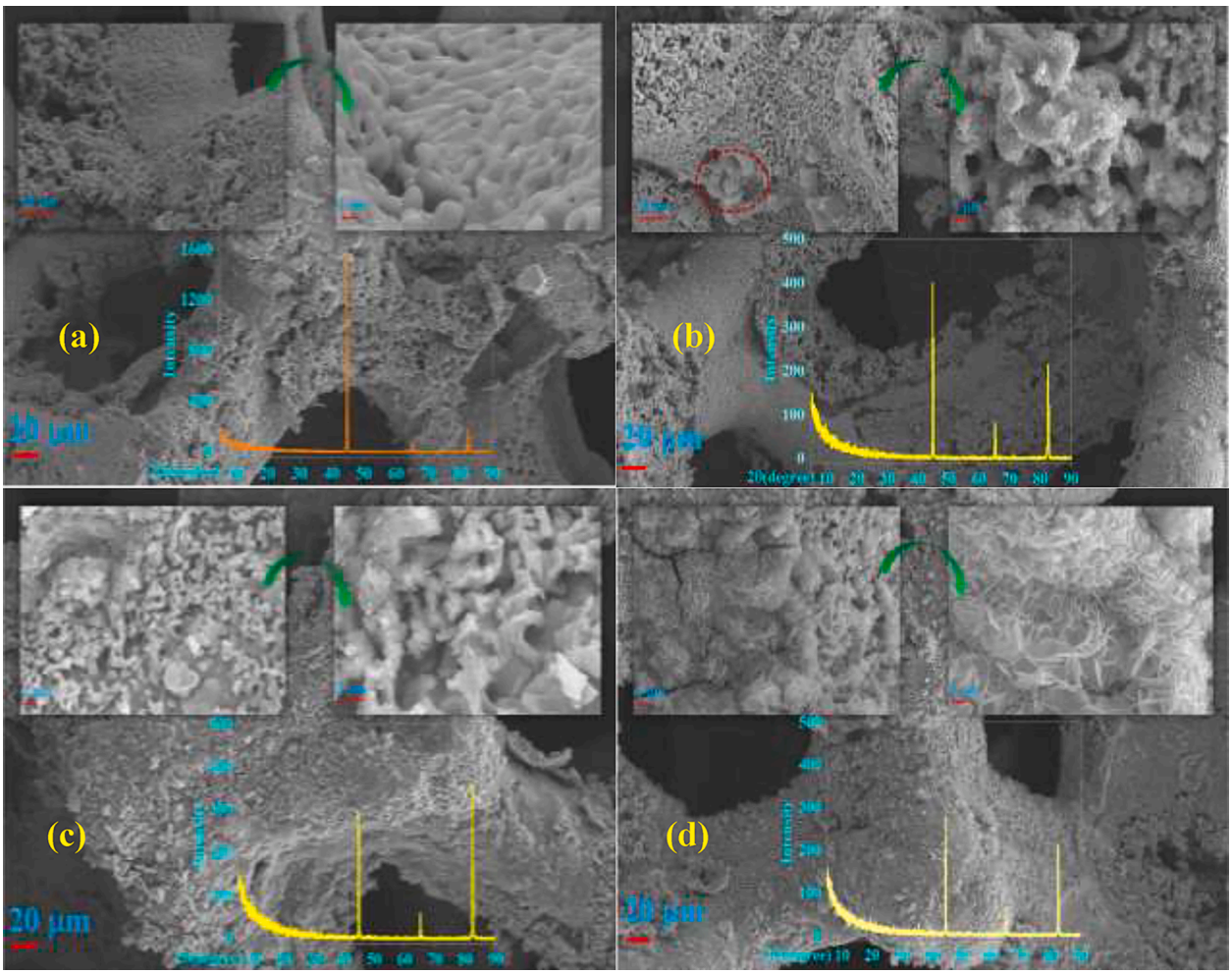

Fig. 3. Comparisons of Fe^0_f with SEM (1 μm, 2 μm, and 20 μm) and XRD (10-90°): (a) original sample without treating, (b) with US-O_{SC} 30 min, and (c) & (d) with O_{SC} but without US, 15 min & 30 min ($_{molar\ ratio}S_2O_8^{2-}/ClO_2^-$ 5:1, f 28 kHz, I 30 W·L^{-1}, pH without adjustment, 0 r·min^{-1}, and initial T 289 K).

dissociation (activated by Fe^0_f under the US roles), but < 1900 K found in the liquid region surrounding the collapsing cavitation bubbles in alkane solvents at 5 Torr vapor pressure under argon [29,30]. As Misik et al. [31] described, the contaminants with different structures may also influence the interface temperature at sonochemical regions.

In addition, the calculated E_a of US/Fe^0_f-O_{SC} was 33.227 kJ·mol^{-1} > 10–13 kJ·mol^{-1}, indicating that degradation process was dominated by an intrinsic chemical reaction rather than a diffusion process. According to study of Cui et al. [32], the modified Freundlich Isotherm (Eq. (22)) could be applied to describe the relationship between the amounts of molecules partitioning (adsorption) at the interface of cavitation bubble and the initial concentration at equilibrium in US-based systems.

$$\log(r_t) = \frac{1}{k_r}\log\left(c_{tpm_{CV,0}}\right) + \log(K_f) \tag{22}$$

where r_t (μM·min^{-1}) was the decomposed rate of tpm_{CV} (Eq. S40), k_r was called as the reactivity constant, and K_f was the adsorption capacity. According to the calculating of r_t, the Section **S11** was presented as the general form.

Therefore, according to US/Fe^0_f-O_{SC}, the log(r_0) vs. log($c_{tpmCV,0}$) had a good liner relation (R^2_{Adj} = 0.996, Fig. 5a), and the $k_{r,0}$, indicating the adsorption intensity, was 0.823, while the $K_{f,0}$, as [32] described, represented the capacity of tpm_{CV} molecules adsorbing or partitioning to the reactive zone (gas–liquid interface) and was 0.0442. Similarly, the $k_{r,end}$ was 0.728, while the $K_{f,end}$ was 0.0659 (R^2_{Adj} = 0.987). By comparison, the adsorption or partitioning capacity of tpm_{CV} to the reactive zone was increased as the degradation progressed.

3.5. Discussion of degradation mechanism induced by US

3.5.1. Contribution of main active species with/without US

The reaction rate of tert butyl alcohol (TBA) vs. •OH (3.8–7.6 × 10^8 M^{-1}·s^{-1}) was much higher than that of TBA vs. $SO_4^{\bullet-}$ (4.0–9.1 × 10^5 M^{-1}·s^{-1}) [33], while the reaction rate of methyl alcohol (MA) vs. •OH (9.7 × 10^8 M^{-1}·s^{-1}) was close to that of MA vs. $SO_4^{\bullet-}$ (2.5 × 10^7 M^{-1}·s^{-1}) [34]. The results of inhibition reactions of different systems with different scavengers were shown in Fig. 5b and Fig. S4. According to Eq. (23), the relative degrees of dependence in •OH or $SO_4^{\bullet-}$ could be obtained.

$$\delta_i = \frac{\Delta k_{obsi}}{k_{obs(none)}} \tag{23}$$

where δ_i represented the shielding effects of different systems with different scavengers, $\Delta k_{obs,\ i}$ represented the difference values of different scavengers, and i represented MA or TBA.

By comparison of δ (MA 6 M, TBA 1 M, relatively enough):

i) δ_{MA}-(Fe^0_f-O_{SC}) (0.692) ≈ δ_{MA}-(O_{SC}) (0.691): both generated •OH and $SO_4^{\bullet-}$ of O_{SC} and Fe^0_f-O_{SC} could be controlled by 6 M MA.

ii) δ_{TBA}-(Fe^0_f-O_{SC}) (0.283) ≪ δ_{TBA}-(O_{SC}) (0.528) but k_{obs}-(Fe^0_f-O_{SC}) > k_{obs}-(O_{SC}): some other active species (maybe $Fe^{IV/V}$) existed.

iii) δ_{MA}-(US-O_{SC}) (0.805) > δ_{MA}-(O_{SC}) and δ_{TBA}-(US-O_{SC}) (0.594) > δ_{TBA}-(O_{SC}): the introduction of US could promote the system to generate

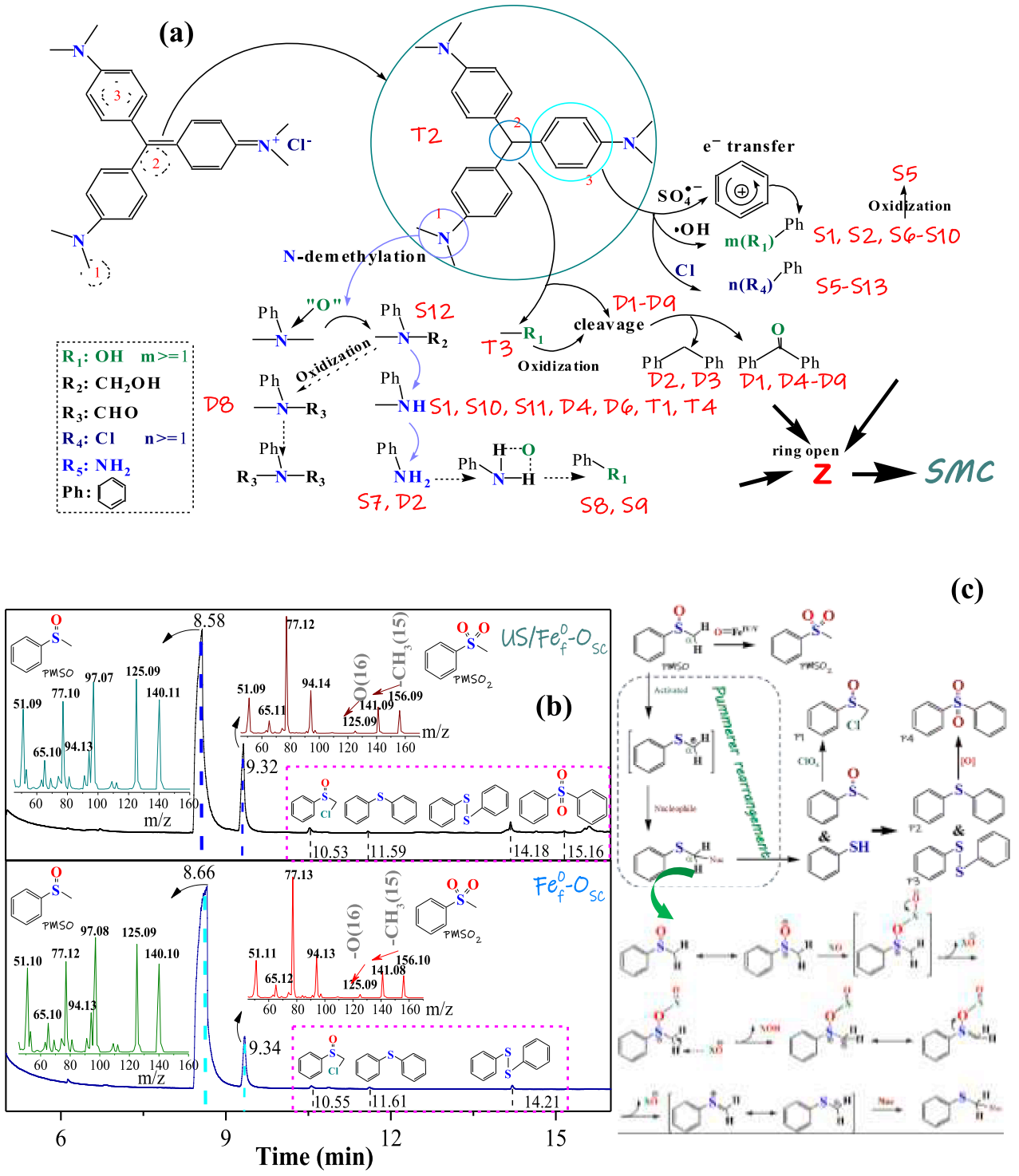

Fig. 4. (a) Comparisons of intermediates detected by GC/MS under different systems and possible degradation pathway of tpm_{CV} on US/Fe^0_f-O_{SC} (S: single benzene ring, D: double benzene rings, T: three benzene rings, Z: straight chain compounds, SMC: small molecule compounds (organic acid, CO_2, H_2O, etc.), the detailed intermediates with t_R and *m/z* seeing in Table S1); (b) GC/MS detection of PMSO and $PMSO_2$ (initial PMSO 6 mM) (the detailed intermediates with t_R and *m/z* seeing in Table 1); and (c) the transformations of PMSO in US/Fe^0_f-O_{SC} and Fe^0_f-O_{SC}.

more both of •OH and $SO_4^{\bullet-}$.

iiii) δ_{MA}-(US/Fe^0_f-O_{SC}) (0.515) < δ_{MA}-(all the others) but δ_{TBA}-(US/Fe^0_f-O_{SC}) (0.643) > δ_{TBA}-(all the others): the •OH and $SO_4^{\bullet-}$ were also the main active species of systems, but the introduction of US tended to promote the active species to transform to more •OH.

3.5.2. *Variation of common Fe and detection of ClO_2 with/without US*

The variations of the dissolved Fe (Fe^{II} and Fe^{III}), suspending Fe & dissolved Fe, and Fe weight loss (suspending Fe, dissolved Fe, and sedimentary Fe) in US/Fe^0_f-O_{SC} were shown at Fig. 5c. The dissolved Fe seemed to exist a dynamic (fluctuant) equilibrium, indicating a ferriki-netics utilization process. By comparisons of Fe^0_f morphology changes among Fe^0_f-O_{SC} and US/Fe^0_f-O_{SC} (SEM, Fig. 3), and Fe^0_f-PDS and US/

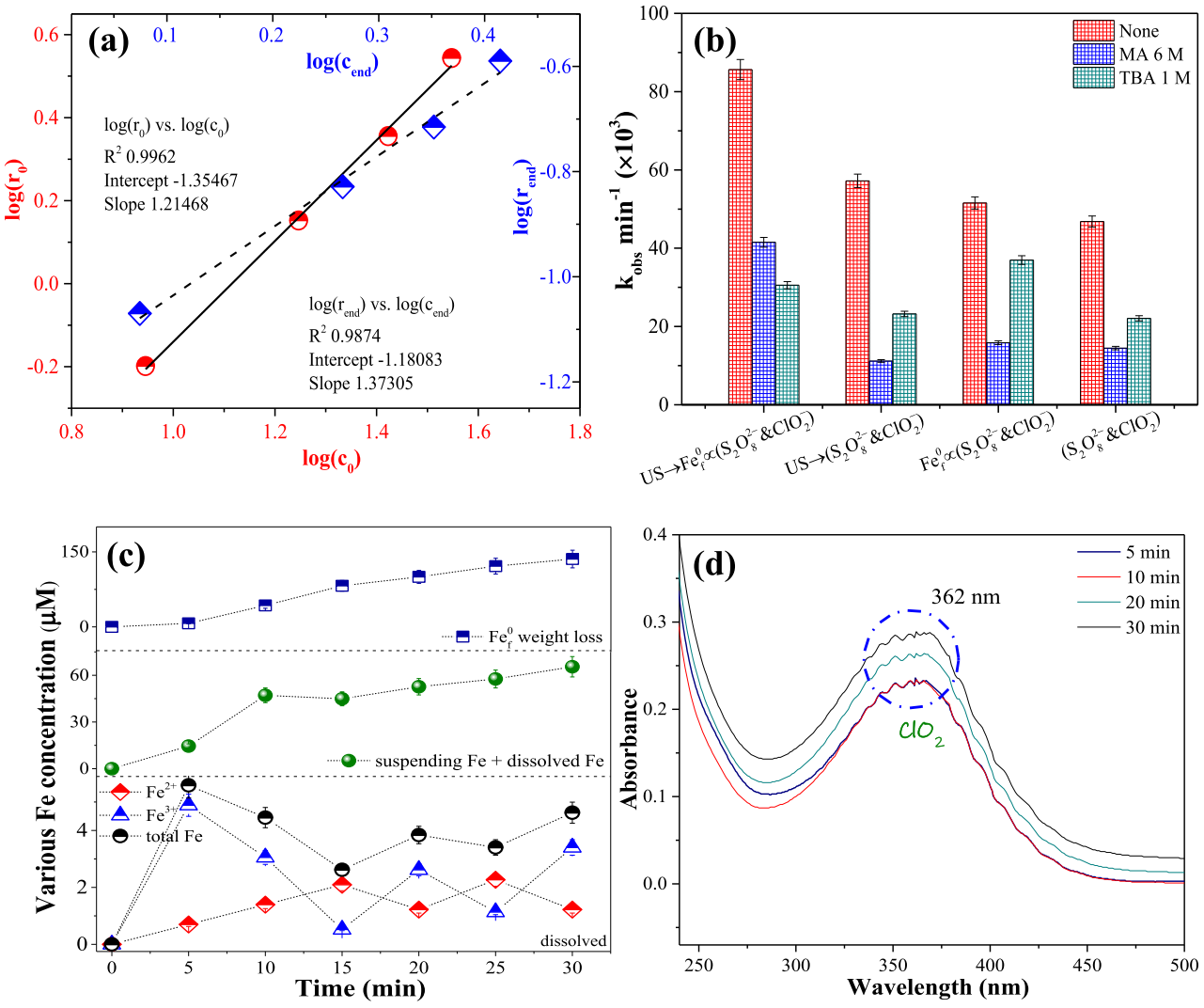

Fig. 5. (a) Freundlich degradation isotherms of tpm_{CV} in Fe^0_f-O_{SC} solution media under US irradiation (f 28 kHz, I 30 W·L^{-1}), (b) inhibition of different systems via screening agents (6 M MA and 1 M TBA), (c) variation of various Fe concentrations in US/Fe^0_f-O_{SC}, and (d) ClO_2 detection of US-O_{SC} by UV–vis spectrum (T 303 K).

Fe^0_f-PDS (previous study), US also had the polishing role in US/Fe^0_f-O_{SC}, but more serious Fe-corrosion in O_{SC} indicated that ferrikinetics may be not sourced from Fe-self circulation (different from PDS), which be mainly attributed to the ClO_2^- role. ClO_2^-/generated-ClO_2 took part in the reaction of Fe, enriching the transformation ways, due to US polishing role, to not only ease Fe^0_f surface passivation but also accelerate Fe^0_f surface corrosion (Fig. 3b). But interestingly, without US polishing, the Fe corrosion and formation process of Fe_xO_y on Fe^0_f surface could be observed under enhanced role of O_{SC} (Fig. 3a smooth → Fig. 3c rough → Fig. 3d "flower"-like). Meanwhile, the relative intensities of characteristic peaks (three) of Fe^0_f were also changed under O_{SC}.

In addition, the ClO_2 was detected by UV–Vis spectrum (ClO_2 different from other chlorines in water, existing absorption peak around 360 nm) [20,21]. From Fig. 5d, the produced ClO_2 presented throughout the reaction process (gradually increasing) on US-O_{SC} by the reaction of Eq. (17). In addition, the anions of $S_2O_8^{2-}$/ClO_2^- after reaction consisted of ClO_2^-, Cl^-, SO_4^{2-}, and a few ClO_3^- (Fig. S5) by IC detection.

3.5.3. ROC-HRMS and EPR detection with/without US

3.5.3.1. ROC-HRMS detection. The spin trapping of DMPO•-SO_4^- was the predominant O-centered adduct for $SO_4^{\bullet-}$, and the adduct could be protonated and decomposed over time to DMPO•–OH [35].

According to US-O_{SC} system (at negative mode), the peak at *m/z* 209 was detected by LTQ and LTQ-Orbitrap, respectively. The MS/MS results of *m/z* 209 in US-O_{SC} system was totally different to those in background, and the peak (*m/z* 209) in background was weak and sporadic but in US-O_{SC} system was stable by parallel experiments, thus indicating that the above peak in background belonged to signal noise but in US-O_{SC} system was a new peak. By MS/MS results, the peak at *m/z* 209 was much close to DMPO•-SO_4^- (Interestingly, the peak at *m/z* 209 being observed in both positive and negative modes with similar but different MS/MS results). Especially, the fragment "*m/z* 97" (failing to capture MS/MS/MS result) in *m/z* 209 in negative mode implied an unstable whole structure just like "-OSO_3(H)" [36–38]. In addition, the unstable peaks at *m/z* 209(+1, +2) with Δ *m/z* (peaks at *m/z* 209(+1, +2) and 112(+1)) around 97(-1, +1), would appear alternately in positive mode (inferring as Scheme 2**b**).

PN-HRMS analysis also confirmed the presence of a peak at *m/z* 130 (only in positive modes) by MS/MS results, which could be explained with DMPO•–OH after abstraction of •H from another molecule in the sample mixture (observed mass was shifted at + 1 Da relative to the mass of DMPO•–OH [39]) (inferring as Scheme 2**a**). Previous studies associated *m/z* 130 with an adduct between the DMPO and •OH [40–42] (Δ *m/z* 18 between *m/z* 130 and 112 representing de –OH and -H),

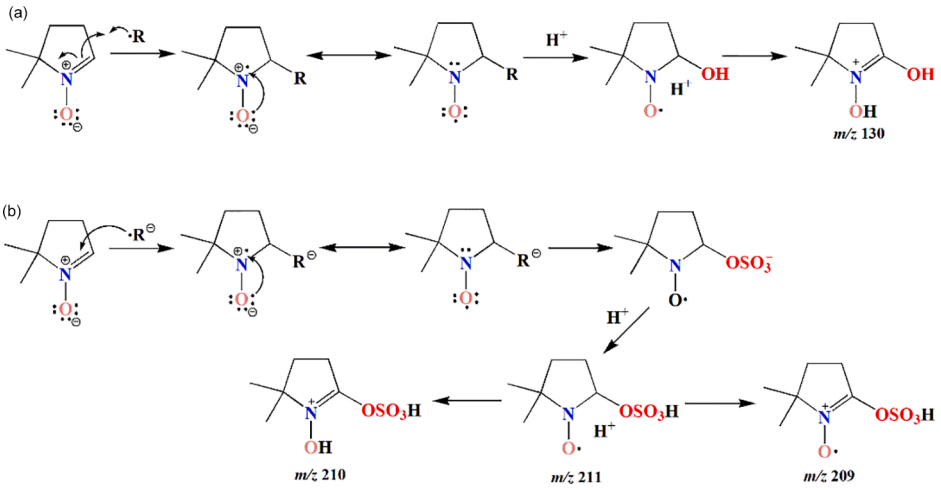

Scheme 2. Transformations of DMPO-R, -R$^-$ [35,40–42].

which was also observed in EPR in our experiments.

As continuous reaction and detection, the peak at *m/z* 209 gradually weakened even disappeared, but the peak at *m/z* 130 enhanced (compared with Fig. 6b & 6d, the peak could be clearly captured in LTQ-Orbitrap over time). Meanwhile, the ESI with the adding MA (compared with Fig. 6c & 6d) attempted to enhance the effect of peaks appearance

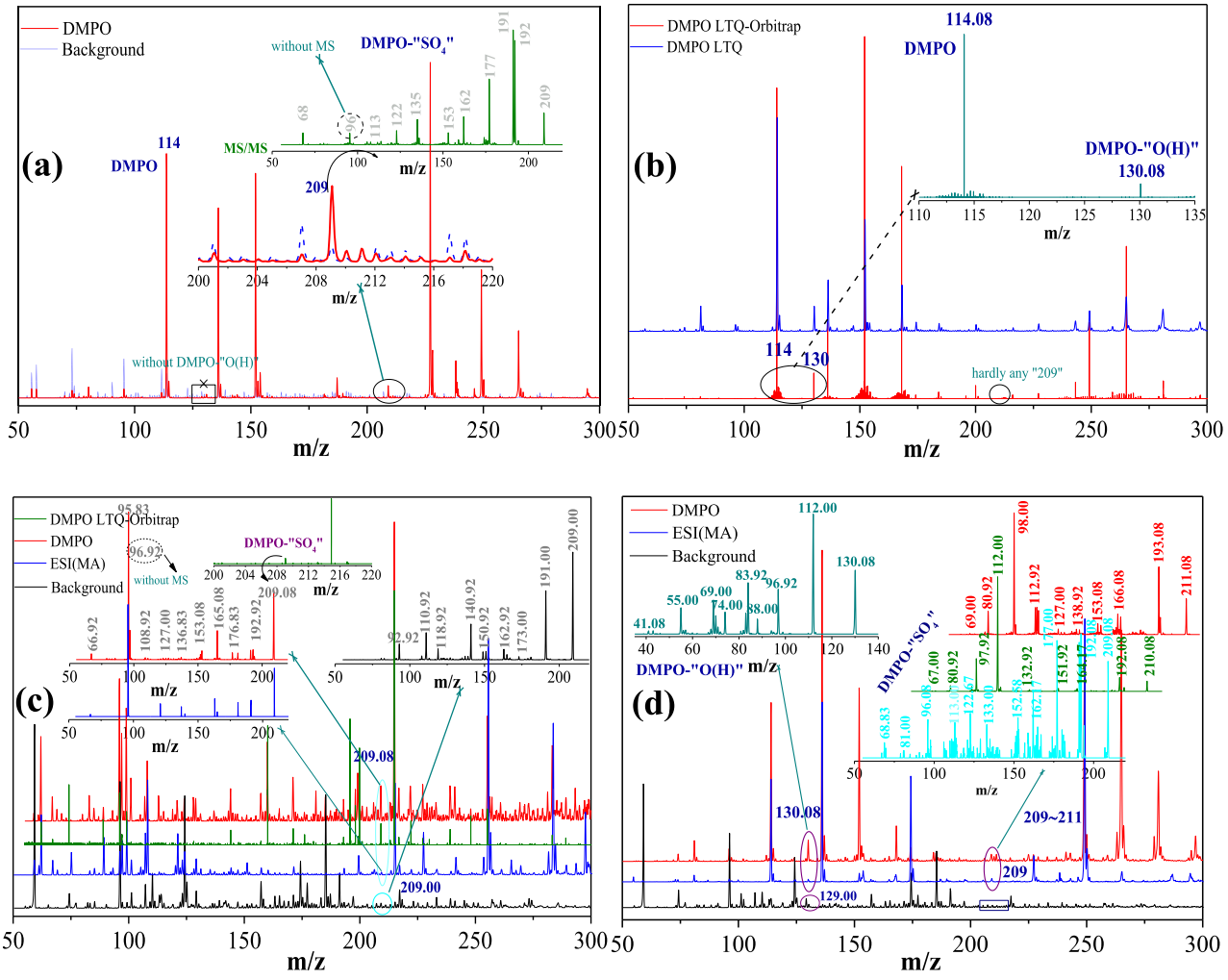

Fig. 6. ROC detection by MS or MS/MS ($_{\text{molar ratio}}S_2O_8^{2-}/ClO_2^-$ 5:1, pH without adjustment): (a) O_{SC}, positive mode, LTQ; (b) US-O_{SC}, positive mode, LTQ& LTQ-Orbitrap (long-time); (c) US-O_{SC}, negative mode, LTQ& LTQ-Orbitrap; and (d) US-O_{SC}, positive mode, LTQ& LTQ-Orbitrap (note: i. operating parameters in Section 2.4; ii. MS/MS results in embedded figure; iii. here presenting comprehensive MS results of continuous period not representing one time point, and continuous period ranging from 3 to 15 min).

but resulted in that peaks at *m/z* 130 and 209 were weaken, and other peaks remained unchanged or indeed enhanced. Herein, two points (mutual supporting) could be further obtained: i) MA indeed could quench both of $SO_4^{\bullet-}$ and •OH; and ii) peaks at *m/z* 130 and 209 most likely corresponded to DMPO•–OH and DMPO•-SO_4^-, respectively.

According to O_{SC} system (Fig. 6a), however, the peak (*m/z* 209) was clearly detected but the peak (*m/z* 130) was hardly detected, suggesting that the main free radicals of O_{SC} were $SO_4^{\bullet-}$. Actually, because of the Scheme 3 [35], the difficulty of free radical identification was increased [43]. However, by PN-HRMS with ROC detecting, the detection (consumption) was along with the reaction (from "without US originally" to "after introducing US") to gain the variations of peaks at *m/z* 130 and 209 in real time, illustrating that i) •OH mainly originated from reaction of US-O_{SC}, not Scheme 3; ii) after introducing US, the type of dominant free radicals tended to be •OH in the system and the transformation may be mainly initiated from $SO_4^{\bullet-}$ (being consistent with Section 3.5.1-iiii); and iii) the PN-HRMS with ROC detecting (comparing with traditional detecting means, liquid chromatograph/mass spectrometer (LC/MS) or EPR with intermittent sample testing one by one) at a certain degree could avoid the potential misjudgement due to Scheme 3.

But most importantly, the ROC-HRMS seemed to prove the radical chain reaction (chain transfer $SO_4^{\bullet-}$ to •OH) directly in the reaction process.

3.5.3.2. EPR signals. The EPR signals of different systems (ClO_2^-, US-ClO_2^-, O_{SC} with different molar ratio, US/PDS, US-O_{SC}, Fe^0_f-PDS, Fe^0_f-O_{SC}, US/Fe^0_f-PDS, and US/Fe^0_f-O_{SC}) were detected to conduct comparative analyses. Commonly, introducing US would not change the peak shapes of EPR signals (e.g. ClO_2^- vs. US-ClO_2^-, O_{SC} vs. US-O_{SC}, Fe^0_f-O_{SC} vs. US/Fe^0_f-O_{SC}, etc.). Differently, single PDS with DMPO would still have the signals, which was consistent with study of Zamora and Villamena [35], possibly due to -OSO_3(H) and –OH.

The DMPO-X_1 (♥) signal with a single nitrogen (a^N = 16.50 G (16.30–16.60), a triplet 1:1:1) [44] may contribute from the oxidation of DMPO itself, but according to study of Kondo et al. [45], peaks labeled "♥" may be due to DMPO•-H adducts showing a primary triplet (a^N = 16.50 G) further split by two secondary hydrogens (⋄, a^H_β = 22.40 G). From Fig. 7a, no •OH signal was observed in ClO_2^- and US-ClO_2^-, however, besides DMPO-X_1 signal, the remaining signal DMPO-X_3 (×) seemed to be closed to ClO• signal [46] and ClO•+Cl• signal [47]; in addition, according to description of Ozawa et al. [48], combining with the DMPO-X_1 and DMPO-X_3, it may contribute from oxidation of spin-traps by ClO_2•; while according to the study of Nishikawa et al. [49], ClO_x (x = 2, 3) radicals led to the above phenomenon. Due to the Cl(III) in ClO_2^-, an intermediate valence [50], it could be explained as ClO_x (x = 0–3) radicals contributed to the above-mentioned results.

In terms of O_{SC} and US-O_{SC}, DMPO-X_1 signal was almost disappeared, the DMPO•-SO_4^- (◆) signal (a^N = 13.78 G, a^H_β = 9.97 G, $a^H_{\gamma1}$ = 1.47 G, $a^H_{\gamma2}$ = 0.98 G) (O-centered adducts) and DMPO•–OH (•) signal ($a^N = a^H$ = 14.91 G, a quartet 1:2:2:1) were clearly obtained. Specially, in terms of relative peak intensity in same spectrum, the relative DMPO•-SO_4^- signals in O_{SC} ($S_2O_8^{2-}$/ClO_2^- 5:1) or after introducing US were more highlighted than that of O_{SC} (1:1) or single PDS, which illustrated co-activation between ClO_2^- and PDS.

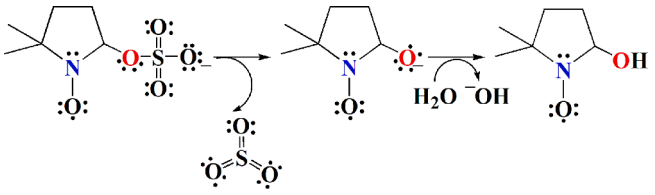

Scheme 3. Intramolecular cleavage decomposition of O-centered sulfate radical adducts [35].

In terms of Fe^0_f-O_{SC} and US/Fe^0_f-O_{SC}, the DMPO•-SO_4^- and DMPO•–OH signals could be still detected but the DMPO-X_1 signal was enhanced obviously, which indicated that the introduction of Fe^0_f accelerated reaction, meanwhile may produce other strongly oxidizing substance besides radicals to result in oxidation of DMPO.

In addition, DMSO as the probe was added the above systems to detect free radicals indirectly [51] due to the reaction of Scheme 4. As the addition of DMSO (Fig. 7b), unfortunately, the •CH_3 signal could not be detected; instead, the quartet signal DMPO-X_2 (* & *, near to 1:1:1:1, $a^N = a^H$ = 14.50 G) appeared (Fig. 7b & 7c). The phenomenon was also observed by Zalibera et al. [52] (the mixtures (DMSO/H_2O) with the lower dielectric permittivity significantly influenced the hyperfine coupling constants and the observed signals largely deviated from typical DMPO•–OH adduct in aqueous media); but it seemed to be consisted with the study of Jiang et al. [53] (contributing from $SO_3^{\bullet-}$ [54] which had be explained by Ranguelova et al. [55]). And according to study of Zamora and Villamena [35], the above quartet signal may source from $SO_3^{\bullet-}$ (S-centered adducts) and •OH with different proportions. In addition, the DMPO•-SO_4^- signal was disappeared, which may result from the competition reaction of DMSO vs. $SO_4^{\bullet-}$ [56].

For comparison, the EPR of Fe^0_f-PDS and US/Fe^0_f-PDS was operated (Fig. 7c). The detected signal of Fe^0_f-PDS was matched to the study of Zhu et al. [57] (adopting Fe-base activation), belonging to "DMPOX", but it seemed to be more closed to composite of DMPO-X_1 and DMPO-X_2 in this study. However, after introducing the US, the signals were complex because of the appearance of DMPO-X_4 (++, ?). Meanwhile, the introducing of Fe^0_f would force and make the EPR signals right-shift and complex (Fe^0_f-O_{SC} vs. US/Fe^0_f-O_{SC}, Fe^0_f-PDS vs. US/Fe^0_f-PDS).

3.5.4. Exploration of US role to O = $Fe^{IV/V}$

Catalytic iron center formed a highly oxidizing oxo-iron species $Fe^{IV/V}$ (namely, O = Fe^{IV} and O = Fe^V) [65] which had the reaction with the sulfoxide in Scheme 5 to generate the corresponding sulfone by oxygen atom transfer step [61,62]. Formally, O = Fe^V was best described as an oxo-Fe(IV)-porphyrin radical cation, namely, O = Fe^{IV}(Por)$^{\bullet+}$ (O = $Fe^{IV\bullet+}$) [65,66]. The PMSO was used as chemical probe in this study, and the methyl phenyl sulfone ($PMSO_2$) with *m/z* of 156, 141, 125, etc. in Table 1 was detected by GC/MS (Fig. 4b), which could demonstrate that the existence of $Fe^{IV/V}$ in Fe^0_f-O_{SC} (t_R 9.34 min) and US/Fe^0_f-O_{SC} (t_R 9.32 min) systems with larger proportion. Meanwhile, it was also corresponding to the aforementioned δ_{TBA} of Fe^0_f-O_{SC} (namely, TBA could not effectively inhibit the degradation). In terms of Fe^0_f-O_{SC} (US/Fe^0_f-O_{SC}) system, the formations of $Fe^{IV/V}$ as shown in Scheme 6, on the one hand, sourced from conversion reaction between "-O-O-" (from PDS) and $Fe^{II/III}$ (from Fe^0) [63,64,66,67]; on the other hand, contributed from adjustment reaction between ClO_2^- and $Fe^{II/III}$ [68], which were operated through a Fe^{II}/Fe^{IV} cycle [65,66,68]. The kinds and relative peak intensities of the intermediates (especially, $PMSO_2$) in US/Fe^0_f-O_{SC} were greater than those in Fe^0_f-O_{SC}, implying that US could facilitate the transformation reaction.

In addition, the detailed information of other formed intermediates P1-P4 was shown in Table 1. PMSO (sulfoxide) would undergo the reaction of "Pummerer rearrangement" to transfer to Ph-thiol (unstable in oxidation system), then further turn into Ph-S-Ph (P2) and Ph-S-S-Ph (P3), meanwhile, P2 would be oxidized into P4 (the detailed process could be seen in Fig. 4c) [69]. In addition, PMSO under the role of ClO_x would turn into P1 via substitution.

3.5.5. Possible degradation process with US

By detected results and literatures, the possible mechanism of degradation process in terms of US/Fe^0_f-O_{SC} was inferred and proposed as follows: at neutral pH, Fe^{IV} would be as the important intermediate in Fenton like reaction [71], but Fe^{IV} would reduce the contribution in ZVI/PDS as result of the decrease of available Fe^{II} [72]. However, US/Fe^0_f-O_{SC} at near-neutral pH still kept well activity, therefore, the introduction of ClO_2^- not only cooperated with PDS to generate co-activation

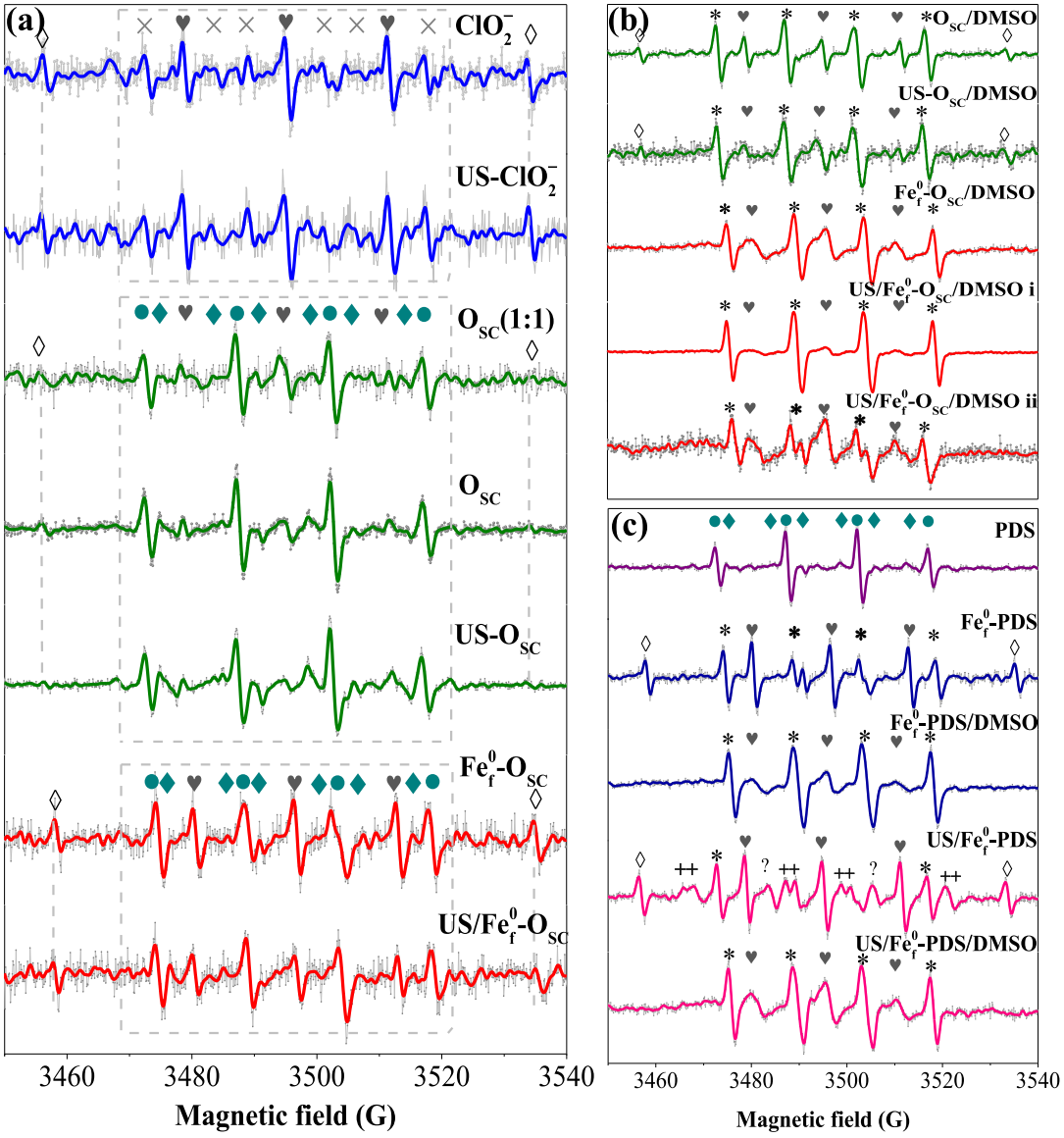

Fig. 7. Comparisons of EPR results under different systems: (a) the step-by-step EPR results of coupled systems, ClO_2^- & US-ClO_2^- 100 mM, DMPO 100 mM, 5 min; $S_2O_8^{2-}$/ClO_2^- 50 mM/50 mM, DMPO 100 mM, 3 min; O_{SC} & US-O_{SC} ($S_2O_8^{2-}$/ClO_2^- 100 mM/20 mM), DMPO 100 mM, 1 min; Fe^0_f-O_{SC} & US/Fe^0_f-O_{SC} ($S_2O_8^{2-}$/ClO_2^- 5 mM/1 mM, Fe^0_f 0.358 mM), DMPO 6 mM, 30 s. (b) the EPR results of O_{SC}-based systems after adding DMSO, O_{SC} (30 s) & US-O_{SC} (5 min) with DMSO ($S_2O_8^{2-}$/ClO_2^- 100 mM/20 mM, DMPO 100 mM, DMSO 100 mM); Fe^0_f-O_{SC} (10 s) & US/Fe^0_f-O_{SC} (i: 1 min, ii: 2 min) with DMSO ($S_2O_8^{2-}$/ClO_2^- 5 mM/1 mM, Fe^0_f 0.358 mM, DMPO 6 mM, DMSO 6 mM). (c) the EPR results of PDS-based systems after adding DMSO, $S_2O_8^{2-}$ 100 mM, DMPO 100 mM, 10 min; Fe^0_f-$S_2O_8^{2-}$ (5 min) and US/Fe^0_f-$S_2O_8^{2-}$ (2 min) ($S_2O_8^{2-}$ 6 mM, Fe^0_f 0.358 mM, DMPO 6 mM, DMSO 6 mM). (◆ DMPO•-SO_4^-, • DMPO•–OH, *(*) DMPO•- SO_3^- & OH, ♥, × & ++ DMPO-Xs, ⋄ DMPO•-H).

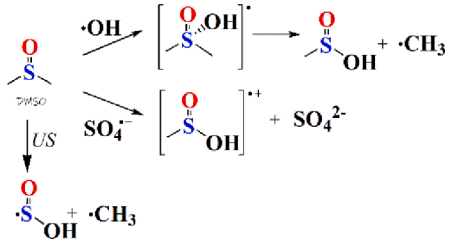

Scheme 4. Reactions of DMSO under •OH, $SO_4^{\bullet-}$, and US in literature reports [56,58–60].

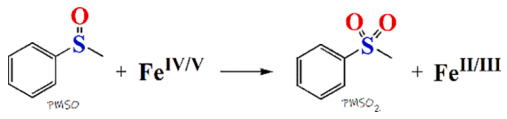

Scheme 5. Reaction between sulfoxides and Fe(IV) in literature reports [61–64].

process ($SO_4^{\bullet-}$ and ClO_2) but also promoted the production and circulation of Fe^{IV} in presence of Fe^0_f (with the cycle of Fe^{II}, Fe^{III}, O = $Fe^{IV\bullet+}$, and O = Fe^{IV}). Meanwhile, US could play another role on the circulation by polishing the surface of Fe^0_f to provide the fresh ZVI source. Meanwhile, the generated $ClO_{x\ (0-3)}$ would accelerate corrosion of Fe^0_f phase interface to release ionic Fe. Importantly, US would also promote

Table 1
The information of generated products after adding PMSO identified by GC/MS.

Intermediates	Retention time (min)		Detected fragments (*m/z*)	*m/z*
	US/Fe^0_f-O_{SC}	Fe^0_f-O_{SC}		
PMSO	8.58	8.66	140 125 97 94 77 65 51	140
$PMSO_2$	9.32	9.34	156 141 125 94 77 65 51	156
P1	10.53	10.55	174 (176) 158 138 125 97 77 51	174
P2	11.59	11.61	186 (187, 188, 185, 184) 152 125 109 84 (86) 77 65 51	186
P3	14.18	14.21	218 (219, 220) 185 154 140 109 84 65	218
P4	15.16	/	218 152 125 97 77 65 51	218

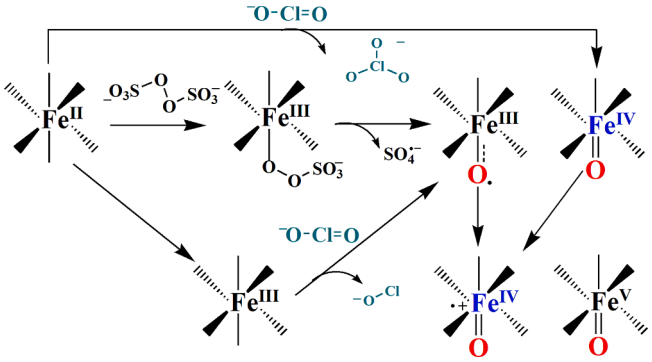

Scheme 6. Reactions of Fe^{II}/Fe^{IV} cycles [63,66,68,70].

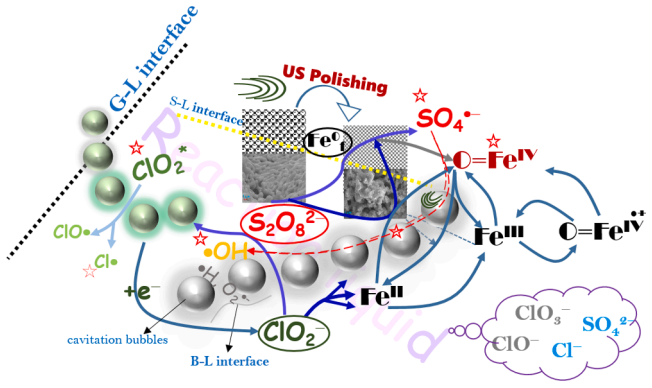

Fig. 8. The possible reaction mechanism of US/Fe^0_f-O_{SC}.

production and transformation of O = $Fe^{IV/V}$, and free radical chain transfer (from $SO_4^{\bullet-}$ to •OH).

The main reaction processes were shown in Fig. 8 and Section **S12**.

3.6. Evaluation of energy consumption based on US

The electrical efficiency per log order (EE/O) was applied to evaluate the application prospect of US/Fe^0_f-O_{SC} (seeing Section **S13** for details). Table S2 listed the calculated EE/O and total cost values of different AOPs for treating wastewater. By economic comparison, the US/Fe^0_f-O_{SC} with EE/O value 13.44 kWh·m^{-3} and total cost value 3.64 \$·m^{-3}.

4. Conclusions

Due to the limitation of ability, the determination (EPR and ROC/MS) of active species in the complex US/Fe^0_f-O_{SC}, and -like systems still face the challenges and should be further explored and analyzed (e.g. isotope detection (^{18}O, ^{17}O, and ^{16}O) or (H, D), etc.). The establishment and calculation of US cavitation model involving bubble–liquid dynamics should be further enhanced.

In this study, the EPR was applied to detect the radicals species of different systems for comparison. The ROC-MS (substitution of EPR) was a preliminary attempt to track the radicals transformation. The US apparent roles to removal reaction were expounded (e.g. de-order reaction, widening the applied range of pH and fluid eddy). The inherent roles of US were stated as follows:

i) US could induce ClO_2^- to co-activate PDS, low the bubble-water interface temperature, and promote the production and circulation of Fe^{II}/Fe^{IV}; ii) US could enrich the kinds of contaminant intermediates, polish the surface the Fe^0_f to avoid surface passivation to provide fresh Fe source, promote the production and transformation of O = $Fe^{IV/V}$, and push free radical chain transfer from $SO_4^{\bullet-}$ to •OH.

In addition, the US/Fe^0_f-O_{SC} may reveal other roles: relatively economical treating cost and potential (ClO_2) disinfection.

Declaration of Competing Interest

The authors declare that they have no known competing financial interests or personal relationships that could have appeared to influence the work reported in this paper.

Acknowledgements

This work was supported by State Key Laboratory of Urban Water Resource and Environment, Harbin Institute of Technology (2019DX08) and National Natural Science Foundation of China (21904029).

Appendix A. Supplementary data

Supplementary data to this article can be found online at https://doi.org/10.1016/j.ultsonch.2021.105750.

References

[1] X.H. Wu, S.Y. Si, W. Tan, X. Lu, F.G. Ye, S.L. Zhao, Preparation of magnetic mesoporous metal-phenolic coordination spheres for extraction of crystal violet and leuco-metabolites in fish, J. Chromatogr. A 1636 (2021), 461776.
[2] S.M. Yakout, M.R. Hassan, A.A. Abdeltawab, M.I. Aly, Sono-sorption efficiencies and equilibrium removal of triphenylmethane (crystal violet) dye from aqueous solution by activated charcoal, J. Clean. Prod. 234 (2019) 124–131.
[3] D. Hurtaud-Pessel, P. Couëdor, E. Verdon, Liquid chromatography-tandem mass spectrometry method for the determination of dye residues in aquaculture products: Development and validation, J. Chromatogr. A 1218 (12) (2011) 1632–1645.
[4] Y. Yu, J. Theerthagiri, S.J. Lee, G. Muthusamy, M. Ashokkumar, M.Y. Choi, Integrated technique of pulsed laser irradiation and sonochemical processes for the production of highly surface-active NiPd spheres, Chem. Eng. J. 411 (2021), 128486.
[5] J. Choi, H. Lee, Y. Son, Effects of gas sparging and mechanical mixing on sonochemical oxidation activity, Ultrason. Sonochem. 70 (2021), 105334.
[6] J. Choi, M. Cui, Y. Lee, J. Ma, J. Kim, Y. Son, J. Khim, Hybrid reactor based on hydrodynamic cavitation, ozonation, and persulfate oxidation for oxalic acid decomposition during rare-earth extraction processes, Ultrason. Sonochem. 52 (2019) 326–335.
[7] J. Theerthagiri, S.J. Lee, K. Karuppasamy, S. Arulmani, S. Veeralakshmi, M. Ashokkumar, M.Y. Choi, Application of advanced materials in sonophotocatalytic processes for the remediation of environmental pollutants, J. Hazard. Mater. 412 (2021), 125245.
[8] J. Lee, U. von Gunten, J.H. Kim, Persulfate-based advanced oxidation: critical assessment of opportunities and roadblocks, Environ. Sci. Technol. 54 (2020) 3064–3081.
[9] Q.H. Xu, F. Shi, H. You, S.T. Wang, Integrated remediation for organic-contaminated site by forcing running-water to modify alkali-heat/persulfate via oxidation process transfer, Chemosphere 262 (2021), 128352.
[10] X. Duan, H. Sun, S. Wang, Metal-free carbocatalysis in advanced oxidation reactions, Accounts Chem. Res. 51 (3) (2018) 678–687.
[11] L.W. Matzek, K.E. Carter, Activated persulfate for organic chemical degradation: A review, Chemosphere 151 (2016) 178–188.
[12] Y.W. Pan, Y. Zhang, M.H. Zhou, J.J. Cai, Y.S. Tian, Enhanced removal of antibiotics from secondary wastewater effluents by novel UV/pre-magnetized Fe^0/H_2O_2 process, Water Res. 153 (2019) 144–159.

[13] J. Wu, J. Zhao, J. Hou, R.J. Zeng, B. Xing, Degradation of tetrabromobisphenol a by sulfidated nanoscale zerovalent iron in a dynamic two-step anoxic/oxic process, Environ. Sci. Technol. 53 (14) (2019) 8105–8114.

[14] Y.W. Wu, X.T. Chen, Y. Han, D.T. Yue, X.D. Cao, Y.X. Zhao, X.F. Qian, Highly efficient utilization of nano-Fe(0) embedded in mesoporous carbon for activation of peroxydisulfate, Environ. Sci. Technol. 53 (2019) 9081–9090.

[15] H.Z. Lv, H.Y. Niu, X.L. Zhao, Y.Q. Cai, F.C. Wu, Carbon zero-valent iron materials possessing high-content fine Fe^0 nanoparticles with enhanced microelectrolysis-Fenton-like catalytic performance for water purification, Appl. Catal. B-Environ. 286 (2021), 119940.

[16] Y.X. Huang, J.W. Jiang, L.M. Ma, Y.W. Wang, M.L. Liang, Z.G. Zhang, L. Li, Iron foam combined ozonation for enhanced treatment of pharmaceutical wastewater, Environ. Res. 183 (2020), 109205.

[17] Z. Wu, Y. Zhao, H. Wu, Y. Gao, Z. Chen, W. Jin, J. Wang, T. Ma, L. Wang, Corrosion engineering on iron foam toward efficiently electrocatalytic overall water splitting powered by sustainable energy, Adv. Funct. Mater. 31 (17) (2021) 2010437, https://doi.org/10.1002/adfm.v31.1710.1002/adfm.202010437.

[18] H. Cosson, W.R. Ernst, Photodecomposition of chlorine dioxide and sodium chlorite in aqueous solution by irradiation with ultraviolet light, Ind. Eng. Chem. Res. 33 (6) (1994) 1468–1475.

[19] N.K.V. Leitner, J. Delaat, M. Dore, Photodecomposition of chlorine dioxide and chlorite by UV-irradiation.1. photo-products, Water Res. 26 (1992) 1665–1672.

[20] R. Hao, X. Mao, Z. Qian, Y.i. Zhao, L. Wang, B.o. Yuan, K. Wang, Z. Liu, M. Qi, J. Crittenden, Simultaneous removal of SO_2 and NO using a novel method of ultraviolet irradiating chlorite-ammonia complex, Environ. Sci. Technol. 53 (15) (2019) 9014–9023.

[21] R.L. Hao, C. Li, Z. Wang, Y.P. Gong, B. Yuan, Y. Zhao, L.D. Wang, J. Crittenden, Removal of gaseous elemental mercury using thermally catalytic chlorite-persulfate complex, Chem. Eng. J. 391 (2020), 123508.

[22] J. Wenk, M. Aeschbacher, E. Salhi, S. Canonica, U. von Gunten, M. Sander, Chemical oxidation of dissolved organic matter by chlorine dioxide, chlorine, and ozone: effects on its optical and antioxidant properties, Environ. Sci. Technol. 47 (2013) 11147–11156.

[23] Q.H. Xu, H.R. Leng, H. You, S.T. Wang, H.Y. Li, Y.B. Yu, A novel co-catalyzed system between persulfate and chlorite by sonolysis for removing triphenylmethane pharmaceutical, J. Environ. Sci. 112 (2022) 291–306.

[24] X. Tan, D. Zhang, K. Parajuli, S. Upadhyay, Y. Jiang, Z. Duan, Comparison of four quantitative techniques for monitoring microalgae disruption by low-frequency ultrasound and acoustic energy efficiency, Environ. Sci. Technol. 52 (5) (2018) 3295–3303.

[25] J. Theerthagiri, J. Madhavan, S.J. Lee, M.Y. Choi, M. Ashokkumar, B.G. Pollet, Sonoelectrochemistry for energy and environmental applications, Ultrason. Sonochem. 63 (2020), 104960.

[26] J. Madhavan, J. Theerthagiri, D. Balaji, S. Sunitha, M.Y. Choi, M. Ashokkumar, Hybrid advanced oxidation processes involving ultrasound: an overview, Molecules 24 (2019) 3341.

[27] Z.S. Wei, F.A. Villamena, L.K. Weavers, Kinetics and mechanism of ultrasonic activation of persulfate: An in situ EPR spin trapping study, Environ. Sci. Technol. 51 (2017) 3410–3417.

[28] R.L. Johnson, P.G. Tratnyek, R.O. Johnson, Persulfate persistence under thermal activation conditions, Environ. Sci. Technol. 42 (24) (2008) 9350–9356.

[29] K.S. Suslick, D.A. Hammerton, R.E. Cline, The sonochemical hot-spot, J. Am. Chem. Soc. 108 (18) (1986) 5641–5642.

[30] K.S. Suslick, Sonochemistry, Science 247 (4949) (1990) 1439–1445.

[31] V. Misik, N. Miyoshi, P. Riesz, EPR spin-trapping study of the sonolysis of H_2O/D_2O mixtures-probing the temperatures of cavitation regions, J. Phys. Chem. 99 (11) (1995) 3605–3611.

[32] D. Cui, A.M. Mebel, L.E. Arroyo-Mora, H. Holness, K.G. Furton, K. O'Shea, Kinetic, product, and computational studies of the ultrasonic induced degradation of 4-methylcyclohexanemethanol (MCHM), Water Res. 126 (2017) 164–171.

[33] P. Neta, R.E. Huie, A.B. Ross, Rate constants for reactions of inorganic radicals in aqueous solution, J. Phys. Chem. Ref. Data 17 (3) (1988) 1027–1284.

[34] G.V. Buxton, C.L. Greenstock, W.P. Helman, A.B. Ross, Critical review of rate constants for reactions of hydrated electrons hydrogen-atoms and hydroxyl radicals ($\cdot OH/\cdot O^-$) in aqueous-solution, J. Phys. Chem. Ref. Data 17 (2) (1988) 513–886.

[35] P.L. Zamora, F.A. Villamena, Theoretical and experimental studies of the spin trapping of inorganic radicals by 5,5-Dimethyl-1-pyrroline N-oxide (dmpo). 3. sulfur dioxide, sulfite, and sulfate radical anions, J. Phys. Chem. A 116 (26) (2012) 7210–7218.

[36] S. Murray, N.B. Rendell, G.W. Taylor, Microbore high-performance liquid chromatography electrospray ionisation mass spectrometry of steroid sulphates, J. Chromatogr. A 738 (2) (1996) 191–199.

[37] D.J. Lamb, H.M. Wang, L.M. Mallis, R.J. Linhardt, Negative-ion fast-atom-bombardment tandem mass-spectrometry to determine sulfate and linkage position in glycosaminoglycan-derived disaccharides, J. Am. Soc. Mass. Spectr. 3 (8) (1992) 797–803.

[38] T.T. Nha Tran, T. Wang, S. Hack, J.H. Bowie, Fragmentations of [M-H](-) anions of peptides containing Ser sulfate. A joint experimental and theoretical study, Rapid Commun. Mass. Sp. 27 (21) (2013) 2287–2296.

[39] C. Giorio, S.J. Campbell, M. Bruschi, F. Tampiere, A. Barbon, A. Toffoletti, A. Tapparo, C. Paijens, A.J. Wedlake, P. Grice, D.J. Howe, M. Kalberer, Online quantification of criegee intermediates of alpha-pinene ozonolysis by stabilization with spin traps and proton-transfer reaction mass spectrometry detection, J. Am. Chem. Soc. 139 (2017) 3999–4008.

[40] Q. Guo, S.Y. Qian, R.P. Mason, Separation and identification of DMPO adducts of oxygen-centered radicals formed from organic hydroperoxides by HPLC-ESR, ESI-MS and MS/MS, J. Am. Soc. Mass. Spectr. 14 (8) (2003) 862–871.

[41] N.A. Bauer, E. Hoque, M. Wolf, K. Kleigrewe, T. Hofmann, Detection of the formyl radical by EPR spin-trapping and mass spectrometry, Free Radical Bio. Med. 116 (2018) 129–133.

[42] P. Domingues, M.R.M. Domingues, F.M.L. Amado, A.J. Ferrer-Correia, Detection and characterization of hydroxyl radical adducts by mass spectrometry, J. Am. Soc. Mass. Spectr. 12 (11) (2001) 1214–1219.

[43] H.-Y. Gao, C.-H. Huang, L.i. Mao, B.o. Shao, J. Shao, Z.-Y. Yan, M. Tang, B.-Z. Zhu, First direct and unequivocal electron spin resonance spin-trapping evidence for pH-dependent production of hydroxyl radicals from sulfate radicals, Environ. Sci. Technol. 54 (21) (2020) 14046–14056.

[44] F.F. Li, L.Q. Xiao, L.J. Liu, Metal-diazo radicals of alpha-carbonyl diazomethanes, Sci. Rep. 6 (2016) 22876.

[45] T. Kondo, V. Mišík, P. Riesz, Sonochemistry of cytochrome c. Evidence for superoxide formation by ultrasound in argon-saturated aqueous solution, Ultrason. Sonochem. 3 (3) (1996) S193–S199.

[46] F. Li, L.W. Sun, Y.B. Liu, X.F. Fang, C.S. Shen, M.H. Huang, Z.W. Wang, D. D. Dionysiou, A ClO center dot-mediated photoelectrochemical filtration system for highly-efficient and complete ammonia conversion, J. Hazard. Mater. 400 (2020), 123246.

[47] Z.X. Zheng, Y.H. Ng, Y.M. Tang, Y.P. Li, W.R. Chen, J. Wang, X.K. Li, L.S. Li, Visible-light-driven photoelectrocatalytic activation of chloride by nanoporous MoS_2@$BiVO_4$ photoanode for enhanced degradation of bisphenol A, Chemosphere 263 (2021), 128279.

[48] T. Ozawa, Y. Miura, J.-I. Ueda, Oxidation of spin-traps by chlorine dioxide (ClO_2) radical in aqueous solutions: First ESR evidence of formation of new nitroxide radicals, Free Radical Bio. Med. 20 (6) (1996) 837–841.

[49] H. Nishikawa, R. Nakamura, Y. Ohki, K. Nagasawa, Y. Hama, Characterization of ClO_x radicals in vacuum-ultraviolet-irradiated high-purity silica glass, Phys. Rev. B 46 (1992) 8073–8079.

[50] J. Marcon, G. Mortha, N. Marlin, F. Molton, C. Duboc, A. Burnet, New insights into the decomposition mechanism of chlorine dioxide at alkaline pH, Holzforschung 71 (2017) 599–610.

[51] B.-Z. Zhu, H.-T. Zhao, B. Kalyanaraman, B. Frei, Metal-independent production of hydroxyl radicals by halogenated quinones and hydrogen peroxide: An ESR spin trapping study, Free Radical Biol. Med. 32 (5) (2002) 465–473.

[52] M. Zalibera, P. Rapta, A. Stasko, L. Brindzova, V. Brezova, Thermal generation of stable spin trap adducts with super-hyperfine structure in their EPR spectra: An alternative EPR spin trapping assay for radical scavenging capacity determination in dimethylsulphoxide, Free Radical Res. 43 (2009) 457–469.

[53] B. Jiang, X.L. Wang, Y.K. Liu, Z.H. Wang, J.T. Zheng, M.B. Wu, The roles of polycarboxylates in Cr(VI)/sulfite reaction system: Involvement of reactive oxygen species and intramolecular electron transfer, J. Hazard. Mater. 304 (2016) 457–466.

[54] T.G. St Denis, D. Vecchio, A. Zadlo, A. Rineh, M. Sadasivam, P. Avci, L. Huang, A. Kozinska, R. Chandran, T. Sarna, M.R. Hamblin, Thiocyanate potentiates antimicrobial photodynamic therapy: In situ generation of the sulfur trioxide radical anion by singlet oxygen, Free Radical Bio. Med. 65 (2013) 800–810.

[55] K. Ranguelova, A.B. Rice, A. Khajo, M. Triquigneaux, S. Garantziotis, R. S. Magliozzo, R.P. Mason, Formation of reactive sulfite-derived free radicals by the activation of human neutrophils: An ESR study, Free Radical Bio. Med. 52 (8) (2012) 1264–1271.

[56] K. Kishore, K.D. Asmus, Radical cations from one-electron oxidation of aliphatic sulfoxides in aqueous solution-a radiation chemical study, J. Chem. Soc., Perkin Trans. 2 (1989) 2079–2084.

[57] K. Zhu, H. Xu, C. Chen, X. Ren, A. Alsaedi, T. Hayat, Encapsulation of Fe^0 dominated $Fe_3O_4/Fe^0/Fe_3C$ nanoparticles into carbonized polydopamine nanospheres for catalytic degradation of tetracycline via persulfate activation, Chem. Eng. J. 372 (2019) 304–311.

[58] S. Fukui, Y. Hanasaki, S. Ogawa, High-performance liquid-chromatographic determination of methanesulphinic acid as a method for the determination of hydroxyl radicals, J. Chromatogr. 630 (1-2) (1993) 187–193.

[59] T. Kondo, L.J. Kirschenbaum, H. Kim, P. Riesz, Sonolysis of dimethyl-sulfoxide water mixtures - a spin-trapping study, J. Phys. Chem. 97 (2) (1993) 522–527.

[60] V. Misik, P. Riesz, Peroxyl radical formation in aqueous solutions of N, N-dimethylformamide, N-methylformamide, and dimethylsulfoxide by ultrasound: Implications for sonosensitized cell killing, Free Radical Bio. Med. 20 (1996) 129–138.

[61] Z. Wang, J. Jiang, S.Y. Pang, Y. Zhou, C.T. Guan, Y. Gao, J. Li, Y. Yang, W. Qu, C. C. Jiang, Is sulfate radical really generated from peroxydisulfate activated by iron (II) for environmental decontamination? Environ. Sci. Technol. 52 (2018) 11276–11284.

[62] O. Pestovsky, S. Stoian, E.L. Bominaar, X.P. Shan, E. Munck, L. Que, A. Bakac, Aqueous Fe-IV=O: Spectroscopic identification and oxo-group exchange, Angew. Chem. Int. Ed. 44 (2005) 6871–6874.

[63] A. Ghosh, D.A. Mitchell, A. Chanda, A.D. Ryabov, D.L. Popescu, E.C. Upham, G. J. Collins, T.J. Collins, Catalase-peroxidase activity of Iron(III)-Taml activators of hydrogen peroxide, J. Am. Chem. Soc. 130 (45) (2008) 15116–15126.

[64] N. Jiang, H.D. Xu, L.H. Wang, J. Jiang, T. Zhang, Nonradical oxidation of pollutants with single-atom-Fe(III)-activated persulfate: Fe(V) being the possible intermediate oxidant, Environ. Sci. Technol. 54 (2020) 14057–14065.

[65] I. Prat, J.S. Mathieson, M. Güell, X. Ribas, J.M. Luis, L. Cronin, M. Costas, Observation of Fe(v)=O using variable-temperature mass spectrometry and its enzyme-like C-H and C=C oxidation reactions, Nat. Chem. 3 (10) (2011) 788–793.

[66] K. Chen, L. Que, Stereospecific alkane hydroxylation by non-heme iron catalysts: Mechanistic evidence for an Fe^{V}=O active species, J. Am. Chem. Soc. 123 (2001) 6327–6337.
[67] H. Li, C. Shan, B. Pan, Fe(III)-Doped g-C_3N_4 mediated peroxymonosulfate activation for selective degradation of phenolic compounds via high-valent iron-oxo species, Environ. Sci. Technol. 52 (4) (2018) 2197–2205.
[68] M.J. Zdilla, A.Q. Lee, M.M. Abu-Omar, Concerted dismutation of chlorite ion: water-soluble iron-porphyrins as first generation model complexes for chlorite dismutase, Inorg. Chem. 48 (2009) 2260–2268.
[69] L. Kurt, B. Czako, Strategic Applications Of Named Reactions In Organic Synthesis, Elsevier, 2005.
[70] L. Xie, X.-P. Zhang, B. Zhao, P. Li, J. Qi, X. Guo, B. Wang, H. Lei, W. Zhang, U.-P. Apfel, R. Cao, Enzyme-Inspired Iron Porphyrins for Improved Electrocatalytic Oxygen Reduction and Evolution Reactions, Angew. Chem. Int. Ed. 60 (14) (2021) 7576–7581.
[71] H. Bataineh, O. Pestovsky, A. Bakac, pH-induced mechanistic changeover from hydroxyl radicals to iron(IV) in the Fenton reaction, Chem. Sci. 3 (5) (2012) 1594, https://doi.org/10.1039/c2sc20099f.
[72] Z. Wang, W. Qiu, S.Y. Pang, Y. Gao, Y. Zhou, Y. Cao, J. Jiang, Relative contribution of ferryl ion species (Fe(IV)) and sulfate radical formed in nanoscale zero valent iron activated peroxydisulfate and peroxymonosulfate processes, Water Res. 172 (2020), 115504.